 Q. J. R. Meteorol. Soc. 141: 2376–2389, July 2015 B DOI:10.1002/qj.2529

RMetS
Royal Meteorological Society

On local and zonal pulses of atmospheric heat transport in reanalysis data

G. Messori* and A. Czaja

Space and Atmospheric Physics Group, Department of Physics, Imperial College London, UK

*Correspondence to: G. Messori, Department of Meteorology, Stockholm University, 16c, Svante Arrhenius väg, 106 91 Stockholm, Sweden.
E-mail: gabriele.messori@misu.su.se

The present study analyses large values (or pulses) of local and zonally integrated meridional atmospheric heat transport due to transient eddies. The data used is the European Centre for Medium-range Weather Forecasts ERA-Interim reanalysis with daily, 0.7° latitude and longitude resolution. The domain of interest is the extratropics. First, the circulation associated with local pulses of heat transport is described. This is found to match many of the features found in warm conveyor belts, although important regional differences exist. The large values of heat transport are seen to be associated with co-varying meridional velocity and moist static energy anomalies. Next, it is shown that there exist strong pulses of meridional heat transport when a zonal integral around a given latitude circle is considered. These zonal pulses are only partly driven by the synchronized occurrence of a large number of local pulses. The existence of such pronounced variability in zonally integrated meridional heat transport can have important consequences for the energy balance of the high latitudes.

Key Words: heat transport; atmosphere; transport pulse; extreme events; reanalysis; variability; transient motions

Received 7 May 2014; Revised 21 January 2015; Accepted 4 February 2015; Published online in Wiley Online Library 02 April 2015

1. Introduction

As part of the vast body of literature dedicated to anthropogenic climate change, a great deal of attention has focused on possible changes in the magnitude and drivers of meridional heat transport (e.g., Hwang and Frierson, 2010; Zelinka *et al*., 2012). Although there is some agreement on the general trends, the transport magnitudes forecasted by models for both pre-industrial and future scenarios are extremely variable (e.g., Donohoe and Battisti, 2012; Zelinka *et al*., 2012).

In many cases, the focus is on zonally integrated, time-mean transport values. The role of variability on subseasonal time-scales has received comparatively little attention. At the same time, atmospheric heat transport is known to be sensitive to short-lived, very intense heat bursts. Swanson and Pierrehumbert (1997) were among the first to highlight the important role played by extreme events in atmospheric heat transport by transient motions, using data from three locations in the Pacific storm track. Messori and Czaja (2013, hereafter MC13; 2014) have generalized this conclusion showing that, at any given location in the extratropical regions during both winter and summer, only a very few days every season can account for over half of the net seasonal transport. The mean transport by transient motions is therefore effectively set by a few extreme events every season.

The above studies focused on a local view of the transport, whereby the calculations were based on transport values at single grid boxes. The discussion was centred on statistical features of the transport and local processes; relatively little attention was devoted to analysing the larger-scale circulation associated with the extremes. If the local extremes were associated with systematic mesoscale, synoptic or larger-scale circulation features, this might lead to a measure of synchronization between events at different longitudes. We will refer to these zonally synchronized events as 'zonal extremes'. Zonal extremes could potentially carry a significant amount of the net seasonal heat transport over a very short period of time. The meridional atmospheric heat transport by transient motions might therefore be characterized by a fundamentally sporadic nature, even when adopting a zonally integrated view. Subseasonal anomalies in the magnitude and convergence of atmospheric heat transport can have severe impacts on the polar regions (Graversen *et al*., 2011). The existence of zonal extremes would therefore provide an important new perspective on the study of meridional heat transport under a changing climate.

If zonal extremes were indeed found to exist, this would open a number of questions: how do local and zonal extremes relate to each other? How will the frequency and intensity of zonal extremes change in the future? How will this influence the polar regions? The present article will focus on the first of these questions, and aims to:

a. Provide a simple overview of the circulation features associated with local extremes.
b. Demonstrate the existence of strong pulses of zonally integrated meridional heat transport across a given latitude circle (i.e zonal extremes).

c. Show that these zonal pulses are partly driven by the synchronized occurrence of a large number of local extremes, and that this is consistent with the circulation features discussed in point (a).

The focus is on atmospheric poleward heat transport by time-dependent motions in the ERA-Interim dataset. An analysis of the climate forecasts made by GCMs is beyond the scope of this study, but the methodology presented here lays out the basis for an investigation on the subject.

First, the circulation associated with local pulses of heat transport is described. This is found to match many of the features found in warm conveyor belts, although important regional differences exist. The second part of the analysis is centred on the largest zonally integrated values of meridional heat transport. It is shown that the top percentiles of the zonally integrated transport distribution are significantly different from all other days, and can therefore be considered zonal extreme events. The discussion focuses on the relationship between these zonal extremes and the local pulses. The structure of this article is as follows. Section 2 describes the data used and outlines the methodology. Section 3 looks at the circulation associated with the local extremes. An analysis of the zonally integrated heat transport is presented in section 4, with a focus on the nature and role of the extreme events. Section 5 discusses the relationship between local and zonal extremes. Finally, section 6 presents some further discussion, conclusions and scope for future research.

2. Data and methods

2.1. The re-analysis data

The present study utilizes the European Centre for Medium-range Weather Forecasts (ECMWF) ERA-Interim reanalysis data (Simmons *et al.*, 2006). Similar to MC13, daily (1200 UTC) fields with a 0.7° latitude and longitude resolution are considered. A subset of the data has been analysed at six-hourly resolution to verify that the conclusions drawn are not dependent on the choice of utilizing daily values. The period taken into consideration spans from June 1989 to February 2011, thereby providing 22 December, January and February (DJF) and 22 June, July and August (JJA) time series. Even though ERA-Interim includes additional years of data, this more limited period is selected to allow for an easy comparison with the analysis presented in Messori and Czaja (2014).

The analysis of the circulation features (section 3) uses all available pressure levels between 975 and 20 mb. The statistical analysis of the extreme events (sections 4 and 5) focuses on the 850 mb level. This is the level of the peak heat transport by transient eddies, and is often used as a reference level in the literature (e.g., Lau, 1978). Other vertical levels in the data set were analysed by MC13 and they found that the 850 mb analysis provided a good indication of the statistics of the transport at other levels.

2.2. Meridional heat transport by transient motions

The transient-eddy transport is computed as the product of v (meridional velocity) and H (moist static energy, hereafter also referred to as MSE) temporal anomalies. These are defined as departures from the linearly detrended seasonal mean, and are denoted by a prime. Velocity is positive polewards in both hemispheres. Moist static energy is defined as:

$$H = L_v q + C_p T + gz, \quad (1)$$

where L_v is the latent heat of vaporization, C_p is the specific heat capacity at constant pressure, T is the absolute temperature, q is the specific humidity, z is the geopotential height and g is the gravitational acceleration (e.g., Neelin and Held, 1987). The anomalies are computed at every grid point for 172 latitude bands between 30°N and 89°N and 30°S and 89°S, and the analysis is performed over both land and ocean.

The terminology 'local event' simply refers to the transport value at a single reanalysis grid box. In order to present results in the same units as the zonally integrated values, the local transport in the figures has been multiplied by the circumference of the latitude at which it is located. Zonally integrated values are computed by integrating each local $v'H'$ value over the width of the grid box it refers to. All the values around a given latitude are then summed to obtain the zonal integral. Both local and zonal values are then normalized by layer thickness, and the transport is expressed in W/1000 hPa. Values therefore can be interpreted as the transport in W that would occur if the local flux were realized at all vertical levels and longitudes.

For both the local and zonally integrated analyses, extreme events are defined as the values of $v'H'$ exceeding the 95th percentiles of the respective distributions, for the full hemisphere and time period considered. Note that these distributions are computed for the 850 mb level only. It is shown by MC13 that the exact percentile chosen as threshold does not affect the statistical characteristics of the extremes for single-point values. The same is found in the case of the zonally integrated distributions. The sensitivity of the analysis to the extreme event threshold is discussed further in section 5.5.

Part of the analysis is performed on time-filtered data. The filter used is a 21-point high-pass finite impulse response filter, with a half-power cut-off at 8 days. It is designed to capture the full breadth of baroclinic time-scales. Chang (1993) suggested that filters with a 6 day cut-off lose a key part of the baroclinic variance. Here, we therefore follow Nakamura *et al.* (2002) in choosing an 8 day cut-off. Where no filter is applied, the analysis encompasses phenomena covering a wide range of periods, beyond those typically associated with baroclinic time-scales. A brief discussion of the sensitivity of the present analysis to filtering is therefore provided in the online Supporting Information (File S2).

The analysis also includes 'well-separated' local extremes. These are local extremes that are driven by distinct atmospheric systems as opposed to extremes resulting from a single, zonally elongated region of enhanced transport, which might register as a local extreme at several locations. In order to provide an objective definition of well-separated extremes, a mean decorrelation length scale for the heat transport is computed at every latitude. The decorrelation scale is defined as the distance over which the autocovariance function of the transport anomalies crosses zero for the first time. Local extremes that are more than one decorrelation scale apart are counted separately. If multiple extremes are within one decorrelation scale of each other, the group is counted only once.

2.3. Two-dimensional heat transport cross-sections

The analysis of the circulation features (section 3) is based on cross-sectional composites of local extreme events in the zonal and height (pressure) plane. The selection of these extremes is based on the transport values at single data points, with no zonal integration applied. In all of the composite figures, only the extremes corresponding to local maxima are selected. If only a simple percentile threshold were applied, an extensive region of strong heat transport could contribute with multiple data points to the statistics. This is desirable when computing, for example, a climatology of heat transport bursts. However, it becomes problematic when analysing atmospheric circulation, because it would artificially replicate the circulation system associated with a single heat transport peak.

In MC13, the majority of local events were found to have zonal wave numbers between 6 and 10. In order to capture the full extent of the extremes, including the surrounding circulation features, 50 reanalysis grid boxes (corresponding to approximately

35° longitude), are retained on either side of the selected local maxima. To avoid double-counting data points, if two extremes occur on the same day and latitude and are less than 100 grid boxes apart, half the grid boxes in the interval are assigned to each of the extremes. The heat transport is then computed across all the selected longitude data points, at all pressure levels. This procedure provides a pressure–longitude transport cross-section for each extreme. All the extremes thus analysed are then composited, and the values found are normalized by the number of data points in the composite. Note that, because some extremes are less than 100 grid boxes apart, the normalization factor will not be uniform across the composite. A similar procedure is applied to obtain cross-sectional plots of the wind fields corresponding to the extreme events. Note that no vertical integration is performed. Indeed, the reanalysis estimates might not be accurate for the whole vertical extent between two adjacent pressure levels. As noted by Trenberth (1991), the values archived in the ECMWF reanalyses should be interpreted as the most accurate values available at those levels, but not representative of layers. Such an issue has vastly improved in the passage from ERA-40 to ERA-Interim, but is still present in the latter data set and should not be ignored (e.g., Graversen *et al*., 2011).

Since the atmospheric circulation is analysed using composite plots, one needs to ensure that the mean picture represents individual events well. As a first step, statistical significance limits are presented in the cross-sectional plots. The null hypothesis is that the structure of the extreme events does not differ significantly from that of all other poleward transport events. Events above the 75th percentile of the full hemispheric distribution are taken as reference for the average event. A random Monte-Carlo sampling (1000 iterations) is then performed to determine locations where the extreme event composite is not statistically different from the average events at the 99% confidence level. A separate test is performed exclusively on the areas that display equatorward (negative) transport. Here, a non-parametric sign test is applied, with the null hypothesis that the data in these regions comes from an unknown distribution with a positive median. Again, a 99% confidence threshold is considered. The first test verifies whether the extreme event composite is statistically different from the weaker poleward transport instances. The second test evaluates whether the negative transport is a robust feature of the extremes or whether it is simply part of a near-zero background flow. The same procedure is applied to the velocity composites.

In addition to this, two further analyses are performed. In the first, extreme events are split into those corresponding to poleward velocity anomalies and those corresponding to equatorward ones. The second analysis focuses on regional domains, selected so as to match the areas in which local extreme events are most frequent. The names of the different domains, and the corresponding geographical boundaries, are listed in Table 1. Figure 6(a) provides a graphical illustration of the same domains.

2.4. Net meridional heat transport and probability density functions

In addition to the transport by transient motions described above, we also briefly analyse the net, vertically and zonally integrated meridional heat transport by all atmospheric motions. This is expressed as:

$$T_{\mathrm{ATM}} = \frac{1}{g}\int_0^1 \mathrm{d}\eta \int_0^{2\pi} \mathrm{d}\phi v\left(\frac{1}{2}\mathbf{u}\cdot\mathbf{u} + C_{\mathrm{p}}T + gz + L_{\mathrm{v}}q\right)\frac{\partial p}{\partial \eta}, \quad (2)$$

where g is gravity, $\mathbf{u} = (u, v)$ is the horizontal wind vector, p is the pressure, ϕ is the longitude and η is the vertical coordinate of the ERA-Interim atmospheric model (Graversen *et al*., 2011). The T_{ATM} provides a value in W for the net northward energy transport across a given latitude circle. A barotropic mass correction is also applied, following Trenberth (1991) and Graversen (2006). This accounts for the non-conservation of mass in the ERA-Interim dataset.

Finally, the present article discusses several probability density functions (PDFs), and refers to their skewness. This is a measure of the asymmetry of a distribution or, more formally, the distribution's third standardized moment. Note that a skewness of zero does not necessarily imply symmetry about the mean. Another oft-used indicator is the most likely value (MLV) of the PDF, which is taken to be the central value of the bin with the highest frequency of events. The exact value of the MLV obviously depends on the choice of bins. Nonetheless, the MLV is generally a robust indicator if used to compare the order of magnitude of the most frequent value of a variable to the one of its most extreme outcomes.

Table 1. Names, abbreviations and geographical boundaries of the domains used in the analysis of extreme event regional composites.

Domain name	Abbreviation	Boundaries
a. Gulf Stream	GS	30°N–55°N; 265°E–335°E
b. Pacific Storm Track	PS	30°N–50°N; 150°E–230°E
c. Bering Strait/Gulf of Alaska	BS	55°N–70°N; 180°E–200°E
d. Nordic Seas	NS	55°N–80°N; 335°E–15°E
e. Southern Ocean	SO	40°S–70°S; 295°E–275°E

3. Atmospheric circulation and local extremes

Previous studies (e.g., Swanson and Pierrehumbert, 1997; MC13; Messori and Czaja, 2014) have highlighted how meridional atmospheric heat transport is sensitive to short-lived, very intense heat bursts. Here, these are referred to as local extreme events (or pulses). The term 'local' simply refers to the transport at a single grid box. When analysing local transport, the extremes form a population of events that are one or more orders of magnitude larger than the MLV of the transport's PDFs. The present section investigates the atmospheric circulation associated with these local extremes.

3.1. Hemispheric composite maps

To investigate the vertical and zonal structure of transient-eddy heat transport extremes, we begin by computing composite transport maps. These take into account extreme events at all available latitude bands (30–89°) over the full analysis period (1989–2011). Figure 1 shows the composite map for events in the Northern Hemisphere during DJF. The other season–hemisphere combinations (not shown) yield similar maps. As would be expected from the definition of extreme events used here, the peak transport is found around 850 mb. The general spatial structure of the extreme events is that of a deep vertical column of poleward transport, flanked by weaker equatorward transport regions to the east and at high levels. Cross-hatching marks the regions where the composite is not statistically different from heat transport events above the 75th percentile of the distribution. The diagonal striping marks regions of equatorward heat transport. The exact position and intensity of the equatorward flow varies significantly between individual events. Sometimes there is virtually no return transport, while at other times a more extended return flow region is seen. At locations where the cross-hatching is superimposed onto the striped regions, the null hypothesis of non-negative transport cannot be rejected, and the equatorward transport is therefore not significant. Notwithstanding the large variability between events, virtually all of the equatorward transport regions are statistically significant. The whole transport pattern displays a small westward tilt, consistent with the typical development of a baroclinic system. Even though the area of poleward heat transport is very extensive, the core of the extreme event is quite narrow, covering only a few degrees longitude on average.

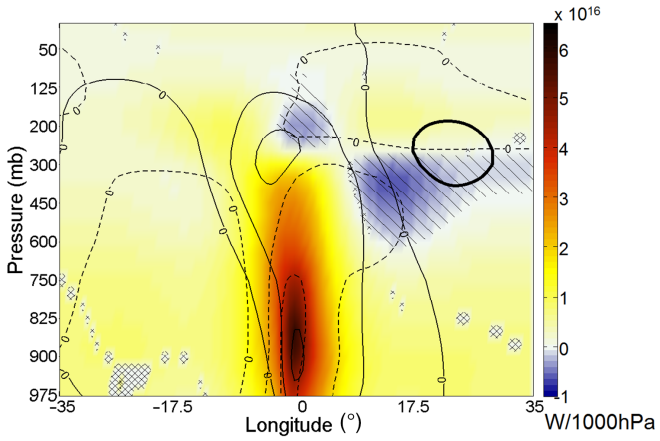

Figure 1. Composite pressure *versus* longitude colour map of meridional heat transport (W/1000 hPa) for extreme events. The diagonal striping marks regions of equatorward transport. The cross-hatching marks regions that are not statistically significant at the 99% confidence level. The continuous contours show meridional velocity anomalies every 2.5 m s^{-1}. The dashed contours show MSE anomalies every 1.5 K. Zero contours for both variables are labelled; thicker contours correspond to negative values. The data cover Northern Hemisphere DJFs from December 1989 to February 2011. All latitude circles between 30°N and 89°N are taken into account. Note that the colour bar is not symmetric about zero.

The spatial scale of the transport is generally in agreement with the conclusions drawn in MC13. The latter study found that the full extent of an extreme event, including the possible recirculation features, typically corresponds to wave number 8 (or, equivalently, 45° longitude).

Figure 1 also displays the composites of meridional velocity (continuous contours) and MSE (dashed contours) anomalies corresponding to the extremes. The strongest positive anomalies in both variables match the peak transport, and the picture across the event core is that of in-phase positive anomalies. As for what concerns equatorward transport, at upper levels it corresponds to negative MSE and positive velocity anomalies, while the opposite sign combination is seen on the eastward flank of the extreme. Finally, the western flank of the extreme events is characterized by a negative MSE anomaly, which is strongest at low levels. Care should be taken in interpreting these results. The contours represent mean anomalies, and the sign of the product of the two means will not always correspond to the sign of the transport, which is the mean of the product.

Next, maps analogous to that in Figure 1 are produced for the individual velocity components, in order to reconstruct the wind field corresponding to the extreme events. Panels (a)–(c) in Figure 2 show the zonal (u) and meridional (v) components of the wind field, as well as the pressure velocity (ω). The figure refers to events in Northern Hemisphere DJF. Meridional, zonal and pressure velocities are positive in the polewards, eastwards and downwards directions, respectively. The diagonal striping marks regions of negative velocities. Cross-hatching marks the regions where the composites are not statistically significant; the null hypotheses adopted are the same as for the heat transport.

Extreme events are characterized by a strongly ascending air stream just to the west of the core of the event ($\omega < 0$), flanked by two regions of subsiding air. The meridional velocity pattern displays a core of strong poleward velocity at the location of the extreme, surrounded by a strong equatorward flow on the eastern flank and a weaker one on the western flank. This is consistent with the velocity anomalies displayed in Figure 1. The zonal flow is eastwards, due to the presence of the midlatitude westerlies. The zonal velocity composite is therefore dominated by the climatological flow rather than by a circulation specific to the extreme events. The statistical significance test, which compares the extreme events to average poleward transport days, is therefore not as relevant as for the other plots, where the major features of the velocity patterns are directly related to the extremes.

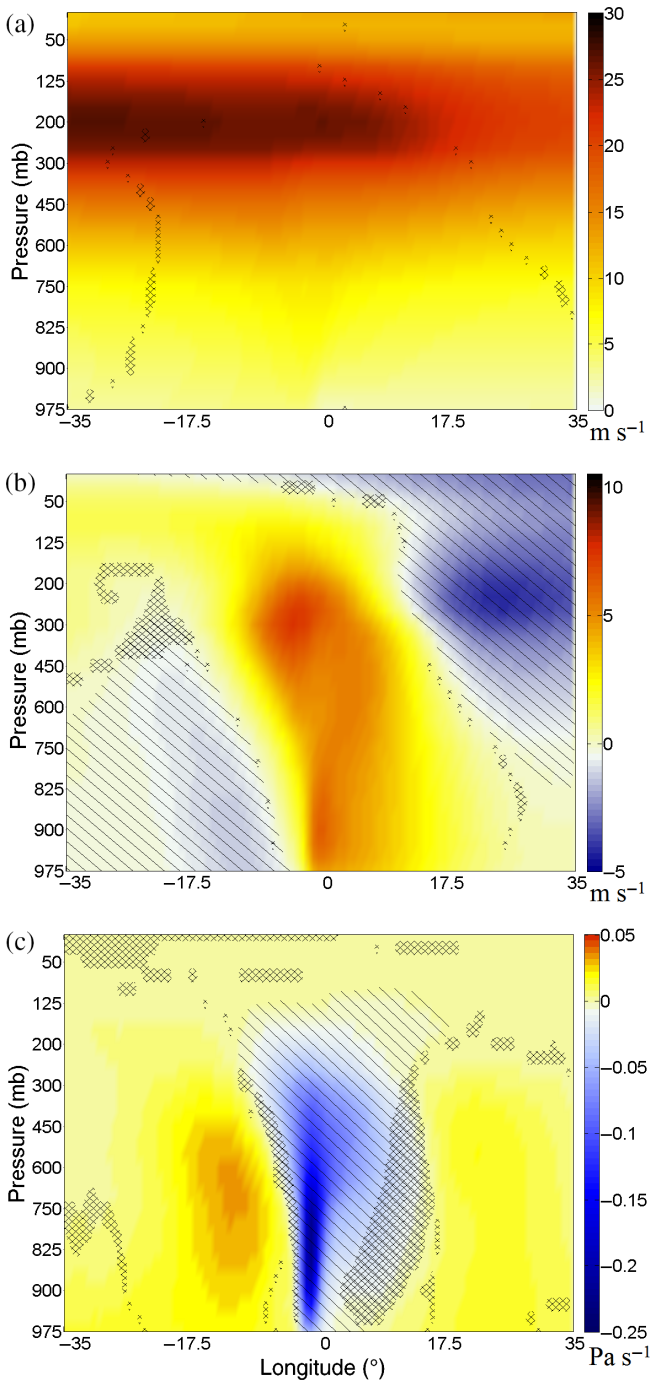

Figure 2. Composite pressure *versus* longitude colour maps of (a) zonal, (b) meridional and (c) pressure velocities for meridional heat transport extreme events. The units are m s^{-1}, m s^{-1} and Pa s^{-1}, respectively. The data cover the same range as in Figure 1. The diagonal striping marks regions of negative velocities (westwards, equatorwards and upwards, respectively). The cross-hatching marks regions that are not statistically significant at the 99% confidence level. Note that the colour bar of (a) is positive-only, whereas those of (b) and (c) are not symmetric about zero.

The large-scale features described above are representative of the majority of events across all four season–hemisphere combinations. However, a composite covering almost a full hemisphere inevitably runs the risk of smoothing out many features, both in the transport and in the anomaly fields. A regional analysis is therefore presented in section 3.2. Further details concerning the variability of the v' and H' signals are also provided in the online Supporting Information (File S1).

3.2. *Cold air advection and regional domains*

The composite in Figure 1 displays a poleward heat transport driven by positive v' and H' anomalies; however, this is not

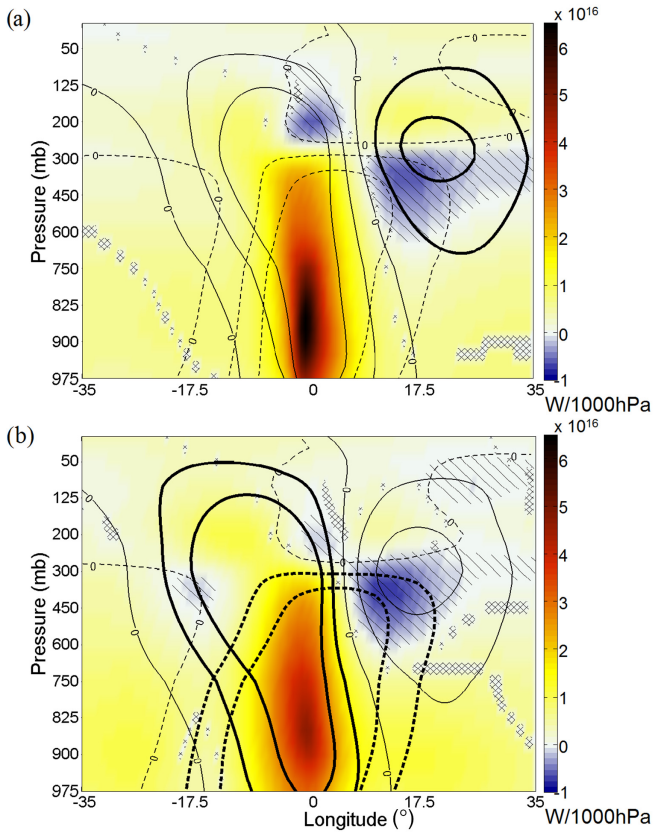

Figure 3. Same as Figure 1 but for extreme events corresponding to (a) positive and (b) negative meridional velocity anomalies at the location of the extreme event local maxima. Unlike in Figure 1, the contour intervals are every 5 m s^{-1} for meridional velocity anomalies and 3 K for MSE ones.

always the case. Indeed, there is a large number of extreme events (approximately 38% of the total in the Northern Hemisphere) where both anomalies are negative, corresponding to equatorward advection of cold air.* This motivates a further analysis, where the extreme events are split into those corresponding to poleward advection and those corresponding to equatorward advection. At the location of the extreme, the transport by definition is poleward; the MSE and velocity anomalies must therefore have the same sign. For conciseness, this section focuses on the winter seasons in both hemispheres.

Figure 3 shows the cross-sectional composites of the extremes corresponding to (a) poleward and (b) equatorward advection. The markings match those in Figure 1, except for the intervals of the v' and H' contours, which are now 5 m s^{-1} and 3 K, respectively. As can be seen, the structure of the transport in the two panels is extremely similar, even though the anomalies driving it are opposite. In turn, both panels bear a strong resemblance to the transport structure seen in the full Northern Hemisphere composite in Figure 1. This highlights two important points. First, that the full hemispheric composite presents a very good representation of the heat transport structure of a typical event, notwithstanding the large domain considered. Second, that similar patterns of heat transport can correspond to very different meridional velocity and MSE anomalies. Further details on the analysis of cold-air advection are provided in the online Supporting Information (File S1).

The presence of extremes driven by both poleward and equatorward advection suggests that large regional differences in the meridional velocity and MSE anomalies may exist. We therefore present a brief analysis of extreme events in the five regions listed in Table 1. Panels (a)–(e) in Figure 4 show the meridional heat transport cross-sections and velocity and MSE anomalies for the five domains. The letters of the panels match those in the table. The colour bars and markings are identical to those in Figure 1. The two Northern Hemisphere storm-track domains (GS and PS, corresponding to panels (a) and (b)) display a structure that is almost identical to that seen in the Northern Hemisphere DJF composite shown in Figure 1. Even the finer details, such as an upper-level local maximum in meridional velocity anomaly, match quite closely. The two sub-Arctic domains (BS and NS, corresponding to panels (c) and (d)) display an overall similar transport pattern, but a weaker transport core. The corresponding meridional velocity and MSE anomalies, even though they are on average both positive at the core, are also significantly weaker. Upon closer analysis this is found to be due to the fact that, in the BS and NS domains, just under half the extreme events correspond to southerly cold-air advection (45 and 44%, respectively). This is in contrast to the GS and PS domains, where the contribution of cold-air advection is significantly smaller (38 and 33%, respectively). As mentioned previously, this compares to a hemisphere-wide average of 38%.

In order to illustrate that both hemispheres present similar features, the regional cross-section for the Southern Hemisphere storm track (SO, panel (e)) is also shown. The transport pattern is broadly similar to that of its Northern Hemisphere counterparts. The only major difference is that none of the equatorward transport is statistically significant. This is mainly due to the fact that the average magnitude of such transport is much smaller than that seen in the Northern Hemisphere.

In both hemispheres, the regional analysis therefore supports the previous conclusion: even though the dynamical drivers of the extreme heat transport events might be very different, the heat transport pattern is surprisingly robust.

3.3. *Physical interpretation*

The results from sections 3.1 and 3.2 show that the heat transport extremes are characterized by a rapidly ascending airstream, and that for the most part they correspond to positive meridional velocity and MSE anomalies. These features account for more than half the heat transport events in all of the domains analysed, although their relative importance is lesser in the more northerly regions such as the Bering Strait and the Nordic Seas. This suggests a direct correspondence with precise mesoscale atmospheric features, such as warm conveyor belts (WCBs) associated with extratropical cyclones. The WCBs are streams of moist, rapidly ascending air parcels that rise from the boundary layer into the upper troposphere. Both their typical duration of a few days and their sporadic occurrence are consistent with the characteristics of the extreme heat transport events (e.g., Eckhardt *et al.*, 2004).

Taking as reference a typical WCB schematic (see Figure 5, corresponding to figure 1 in Catto *et al.* (2010), adapted from Browning (1997)), the rapid ascent near the location of the extremes would match the warm conveyor itself. The fact that the highest rate of ascent is seen to the west of the 850 mb heat transport core is consistent with the flow of the warm conveyor turning anticyclonically as it gains height. The descending motion seen in the velocity composites would correspond to the dry air from the upper atmosphere on the western flank of the WCB. Indeed, as shown in Figure 1, this flow mostly corresponds to a negative MSE anomaly. Such an anomaly is particularly intense in the two Northern Hemisphere storm-track domains. What the WCB schematic does not necessarily explain is the fact that the return heat transport is generally seen only on the eastern flank of the extremes. In fact, idealized simulations of midlatitude cyclones predict two recirculating branches of the WCB, one to the east and one to the west of the location of rapid ascent (e.g., Boutle *et al.*, 2010). A further element that is not present in the heat transport composites is the cold conveyor belt (CCB). This is a cold air feature typically seen to the west of the WCB.

*Even though we are analysing velocity anomalies as opposed to absolute values, for ease of reference we term the instances where v' is negative as equatorward advection and those where it is positive as poleward advection.

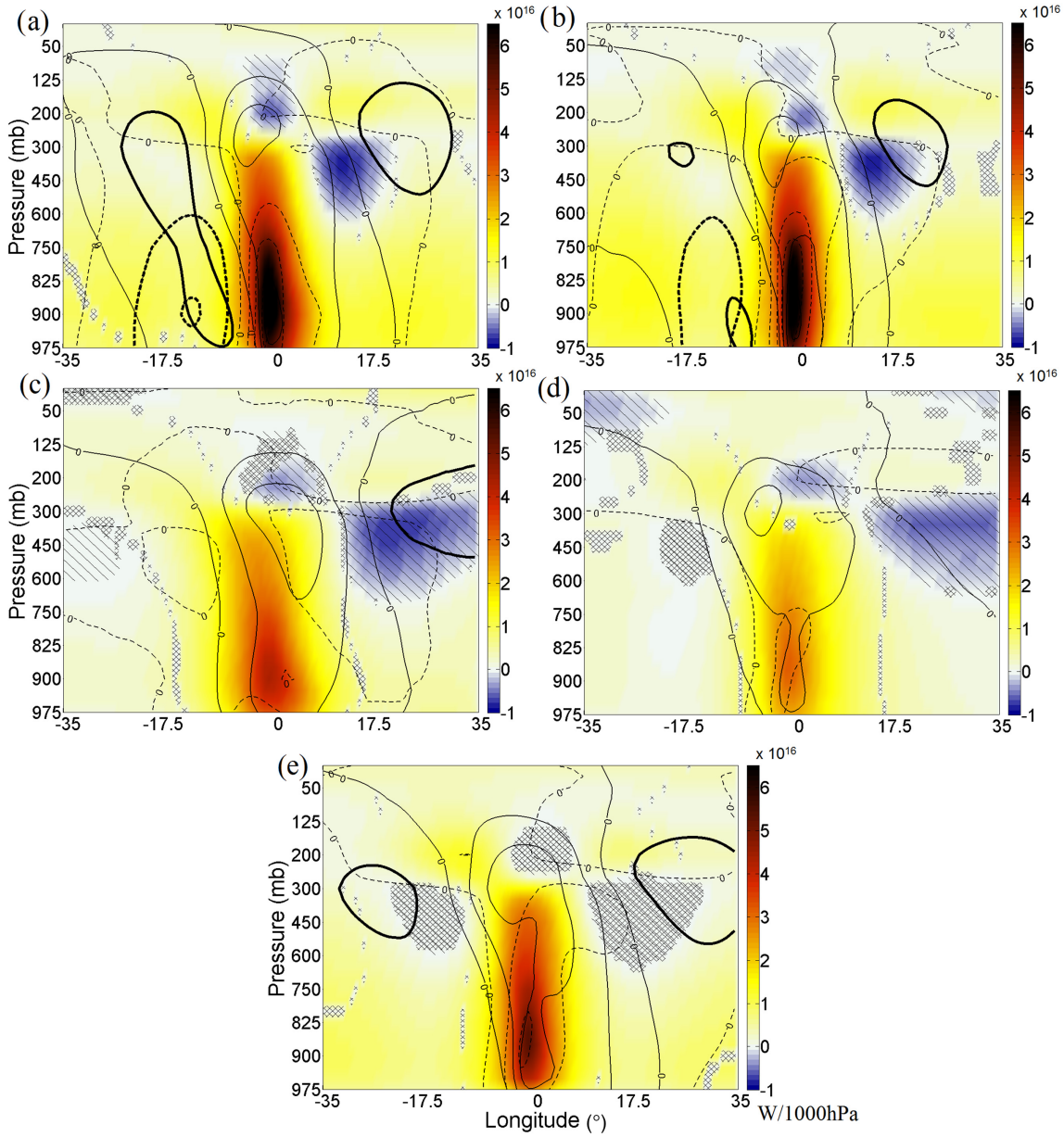

Figure 4. Same as Figure 1 but for extreme events in the five regional domains listed in Table 1. The letters of the panels match those in the table.

These discrepancies between the structures of the heat transport extremes and of the WCBs suggest that the latter do not drive the totality of the extremes. Indeed, almost 40% of the selected events correspond to cold air advection. Consequently, the exact structure of the velocity and MSE anomalies varies significantly across the different individual events, and some do indeed agree closely with the typical recirculation pattern seen in WCBs. The GS composite (Figure 4(a)), for example, displays a low-level region of negative v' and H' to the west of the extreme event core, consistent with a recirculating CCB-type feature.

The climatologies of local extreme heat transport events (Figure 6(a)) and WCBs (Figure 6(b), originally figure 3(f)) from Eckhardt *et al.*, 2004), display some differences in the geographical distributions. There is a good match between WCBs and extreme heat transport events over the storm-track domains, but elsewhere the two distributions do not overlap as closely. Examples of this are over the Bering region and in the Nordic Seas, where relatively few WCBs are detected, even though there are significant numbers of heat transport extremes. In these regions, the mean structure of the heat transport extremes shows fewer resemblances to WCBs than in the storm-track domains. A comparison with WCB climatologies from other studies, such as Madonna *et al.* (2014), presents a very similar picture.

A possible analogue for the negative v' events could be provided by marine cold-air outbreaks (MCAOs). These are large-scale outflows of cold air masses over the ocean, and would correspond to negative v' and H' values. The Northern Hemisphere MCAOs are particularly intense in three regions: the Nordic Seas, the Labrador Sea and the Northern Pacific (e.g., Kolstad and Bracegirdle, 2008). Two of these regions match the NS and BS domains, where the cold advection events are most frequent. In both the full Northern Hemisphere domain and the regional composites, these events are fewer than the WCB-type structures, and are therefore smoothed out. Obviously, the v' and H' patterns of the cold-air advection extremes are very different from those of the mean depicted in Figure 1. However, the typical heat transport structure is surprisingly similar, as illustrated in Figure 3(b).

An important question that has not been fully addressed concerns whether the circulation described above is indeed unique to the highest percentiles of the distribution, or whether the so-called 'extremes' are not that different from median days in terms of the circulation pattern. Composite cross-sections of the lower percentiles of the distribution (not shown) are found to lack the rapid ascent and return flows seen in the extreme event plots. Even composite plots of events in the top 10 percentiles present some differences compared with Figure 1, most notably in the

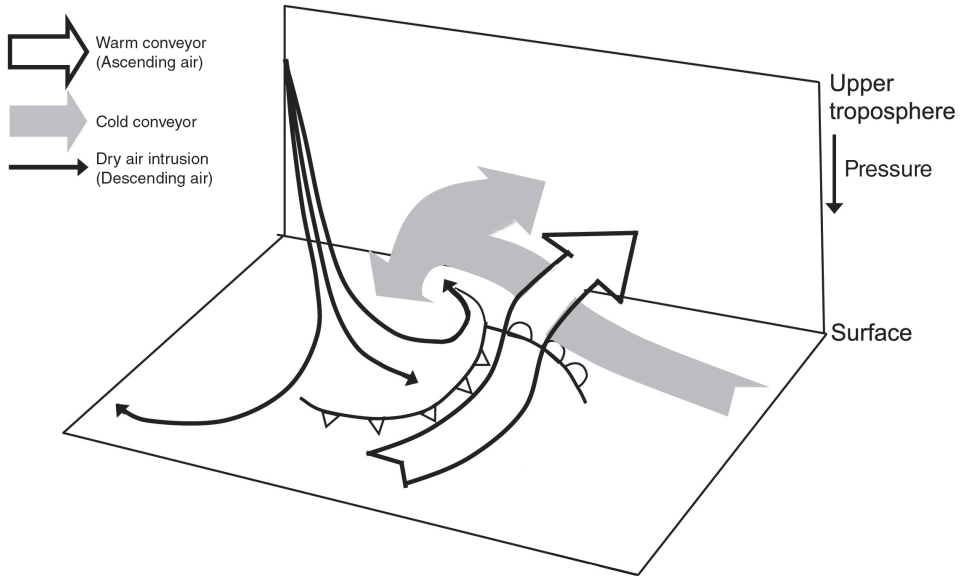

Figure 5. Schematic showing the typical structure of a conveyor belt system, including the warm conveyor, the cold conveyor and the dry air intrusion (from Catto *et al.*, 2010, © American Meteorological Society, used with permission).

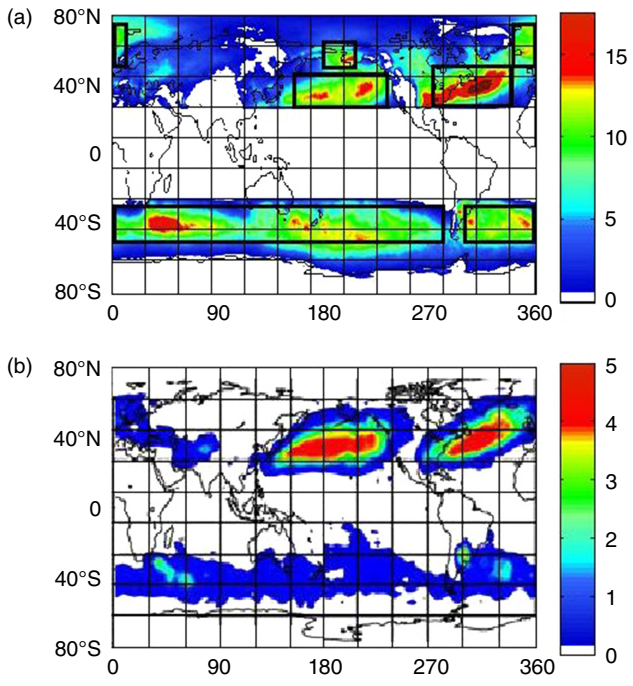

Figure 6. (a) Map of seasonal mean spatial distribution of local heat transport extreme events for DJF. The data cover DJFs from December 1989 to February 2011. The scale of the colour bar corresponds to the number of data points per season per 0.7° × 0.7° box. The calculation is not applied equatorward of 30° latitude. The black boxes correspond to the regional domains used in section 3.2. The exact coordinates for each domain are listed in Table 1. (b) Map of seasonal mean spatial distribution of WCB trajectories 24 h after genesis for DJF. The data cover DJFs from December 1979 to February 1993. The scale of the colour bar corresponds to the fraction (in per cent) of all trajectories that fulfil the WCB criteria (from Eckhardt *et al.*, 2004, © American Meteorological Society, used with permission).

return flows. This is in agreement with the fact that the extreme event composites are statistically different from events above the 75th percentile at most points in the cross-sectional composites. The structure described above is therefore specific to the upper percentiles of the $v'H'$ distribution, and justifies the terminology adopted thus far.

4. The zonal mean view

We now shift our attention to the extremes (or pulses) in zonally integrated heat transport, which have received less attention in the literature. By zonally integrated transport, what is intended here is simply the single grid-box transport integrated around full latitude circles.

4.1. *Zonally integrated heat transport PDFs*

As first step, we analyse the PDFs of zonally integrated heat transport in the ERA-Interim dataset. The aim is to verify whether the top percentiles of the data play any relevant role in setting the net seasonal transport. The net seasonal transport is taken to be the integral of the distribution for the full spatial and temporal domains being analysed. In constructing the PDFs, the integral of the heat transport around a latitude circle, on a given day, is treated as a single data point. All available latitude bands (30–89°) and years (1989–2011) are considered. In the interest of conciseness, the resulting distributions are shown only for Northern Hemisphere DJFs and Southern Hemisphere JJAs (Figure 7(a) and (b), respectively).

The PDFs are significantly different from those obtained by MC13, which were constructed by treating the transport at each grid box as a single data point. For comparison, the single-point distribution for Northern Hemisphere DJF is shown in Figure 8(a). Its Southern Hemisphere counterpart is very similar. Both Figures 7 and 8(a) consider the same data set and geographical domain. Figure 8(a) illustrates two salient features of the single-point distributions: a very pronounced MLV and a thin, extended positive tail. This tail represents a very small fraction of the overall data, as shown by the cumulative distribution function (CDF) overlaid onto the PDF. However, it accounts for a significant part of the net seasonal transport. The distributions also have a large skewness (4.8 for Northern Hemisphere DJF).

The zonally integrated distributions shown in Figure 7 still have a well-defined MLV and long positive tails. However, these tails account for a much larger fraction of the events than was seen in the single-point distributions. Furthermore, the skewness values are significantly lower than those of the single-point data (0.83 *versus* 4.8 for Northern Hemisphere DJF), and the two hemispheres present important differences. The strong positive year-round atmospheric heat transport suggests that negative transport values should be almost entirely absent. It is therefore interesting to note that both hemispheres display some negative values, albeit with very low frequencies and magnitudes. These events are briefly addressed in section 4.2. The MLVs of both hemispheres lie in the smallest positive bin of the respective distributions, centred on zero. The fact that both hemispheres

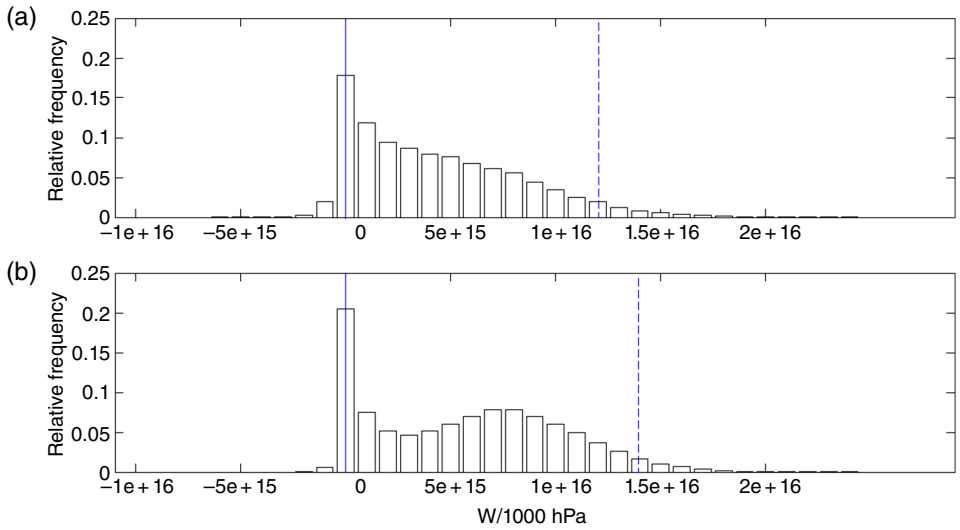

Figure 7. The PDFs of zonally integrated atmospheric heat transport due to transient eddies for (a) Northern Hemisphere DJFs and (b) Southern Hemisphere JJAs. Both PDFs are plotted over the same bins. The data cover the 850 mb fields from June 1989 to February 2011. All latitude circles between 30°N and 89°N and S are taken into account. The skewnesses of the PDFs are (a) 0.83 and (b) 0.34. The corresponding most likely values are (a) 0 W/1000 hPa and (b) 0 W/1000 hPa. The continuous vertical lines show the bins corresponding to the most likely values. The dashed vertical lines show the bins corresponding to the 95th percentiles.

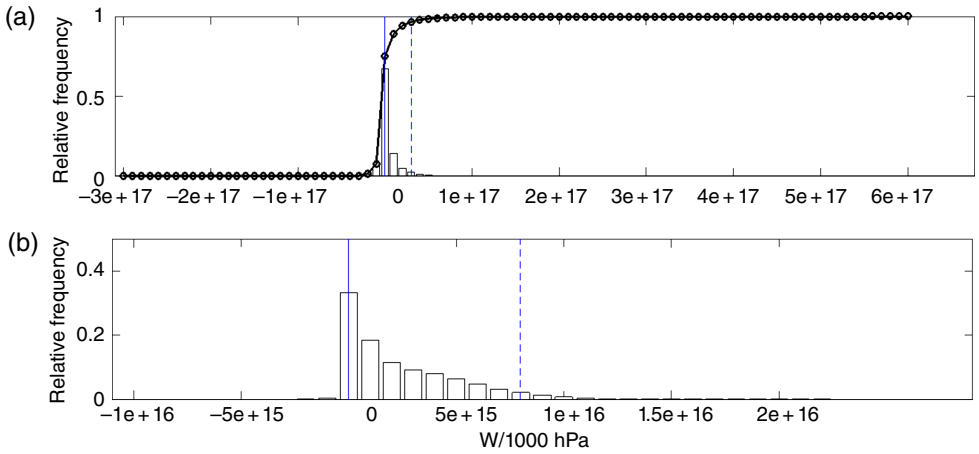

Figure 8. The PDFs of (a) local and (b) high-pass filtered zonally integrated atmospheric heat transport due to transient eddies. The data cover Northern Hemisphere DJFs from December 1989 to February 2011. All latitude circles between 30°N and 89°N are taken into account. The skewnesses of the PDFs are (a) 4.8 and (b) 1.34. The corresponding most likely values are (a) 0 W/1000 hPa and (b) 0 W/1000 hPa. The continuous vertical lines show the bins corresponding to the most likely values. The dashed vertical lines show the bins corresponding to the 95th percentiles. The continuous black line with circular markers in (a) shows the CDF of the data.

have exactly the same MLV, and that such MLV is equal to zero, is simply due to the choices of plotting both distributions over the same bins and of centring a bin on zero. As the MLV is defined here as the central value of the bin with the highest frequency of events, as long as both distributions have similar peaks in frequency, the resulting MLVs will be identical unless the bins are very narrow. Further analysis shows that the majority of the values lying in the bins centred on zero are positive.

Concerning the differences between hemispheres, the most striking is the bimodality of the Southern Hemisphere PDF. By splitting the distribution into two latitude bands (30–60°S and 60–89°S, not shown), it becomes clear that the lower latitudes account for the right-hand side peak, while the higher latitudes account for that on the left-hand side. This is partly due to the lower relative frequency of extremes in the high latitudes: the pronounced near-zero MLV of the PDF is driven by the very high latitudes, where few 850 mb extremes are seen. A similar pattern is seen in the Northern Hemisphere, but the split between the two latitude bands is less marked, and thus does not lead to a bimodal distribution. Further discussion of the differences between the two hemispheres is presented in section 6. The PDFs for Northern Hemisphere JJA and Southern Hemisphere DJF share the same qualitative features as their wintertime counterparts, albeit with some quantitative differences.

4.2. *Equatorward transport events*

As mentioned in section 4.1, the PDFs of the zonally integrated transport display some negative values. These equatorward transport events correspond to between 6.3 and 8.9% of the data points, depending on the hemisphere and season. The values for all four cases are shown in Table 2. These numbers would not be surprising for single-point transport values, but they are intriguing for the zonally integrated case, where some measure of compensation between different longitudes may be expected.

From a dynamics standpoint, it is interesting to analyse the role of the different time-scales in driving this negative transport. Figure 8(b) displays the zonally integrated heat transport distribution for the high-pass filtered Northern Hemisphere DJF data. This can be compared with Figure 7(a), which displays the same distribution for the unfiltered data, plotted using the same bins. Focusing on the negative portion of the distribution, it can be seen that the values in the filtered data are greatly reduced in magnitude. The lowest filtered values are less than 30% of the magnitude of the lowest unfiltered ones, and the fully negative bins in Figure 8(b) are almost completely depopulated. This probably reflects the fact that motions in the high-pass band are the ones 'tapping' into the available potential energy of the atmosphere, lowering its centre of mass and, as a result, carrying heat polewards. The reduction in negative values is much

Table 2. Frequency of equatorward zonally integrated atmospheric heat transport values. The 850 mb column refers to events where the zonally integrated transport by transient motions is equatorward at 850 mb. The 850 and 300 mb column refers to events where the zonally integrated transport by transient motions is equatorward at both 850 and 300 mb. The 850 mb and full transport column refers to events where the zonally integrated transport by transient motions at 850 mb and the vertically and zonally integrated net transport by all motions are both equatorward. The data cover all longitudes and latitudes, from 30°N to 89°N and from 30°S to 89°S over the period June 1989–February 2011.

Hemisphere	Season	Equatorward transport events (%)		
		850 mb	850 and 300 mb	850 mb and full transport
Northern	DJF	8.9	4.7	1.2
	JJA	6.3	2.6	1.4
Southern	DJF	8.6	5.5	2.1
	JJA	6.3	3.6	0.8

sharper than that seen for the positive tail of the distribution, and suggests that the zonally integrated equatorward transport is primarily driven by low-frequency motions. The increase in skewness (1.34 *versus* 0.83) confirms this. In fact, the skewness provides a measure of the asymmetry of a distribution; in this case the higher skewness of the filtered data corresponds to more unequal positive and negative tails. This point is discussed further in section 6.

Returning to the unfiltered data, an obvious question to ask is whether transient motions at other pressure levels act to balance out the negative contribution of the 850 mb level. To obtain an indication of this we extend our analysis to the 300 mb level, which is the approximate level of the secondary peak in meridional heat transport by transient motions (Peixoto and Oort, 1992). Depending on the season and hemisphere, it is found that between 41.6 and 63.6% of the equatorward transport data points identified at 850 mb also display a negative transport at 300 mb. Therefore, up to 5.5% of the data points present an equatorward transport at both levels. This suggests that the transport by transient motions displays a strong vertical coherence in a zonally integrated sense. Again, the values for all four season–hemisphere combinations are displayed in Table 2.

A similar calculation can be applied to the net meridional energy transport. By 'net' here we indicate the zonally and vertically integrated meridional atmospheric energy transport by all motions. It is found that between 12.3 and 23.9% of the data points where the zonally integrated 850 mb transport is negative correspond to a negative net transport. This implies that typically 1–2% of the data points display an equatorward net atmospheric heat transport, with a contribution from transient motions at 850 mb. In these instances, the atmosphere as a whole carries energy towards the Equator. As might be expected, the higher percentages correspond to the summer seasons of the two hemispheres, when the climatological poleward transport is weaker (see Table 2).

4.3. *The role of zonal extreme events*

A visual assessment of the PDFs in Figure 7 suggests that the contribution of the largest zonal events to the overall transport is significantly lower than that seen in Figure 8(a) for the local extremes. The contributions of the top 5% of events in the zonal transport PDFs to (i) the overall and (ii) the poleward-only transports are shown in Table 3. The values displayed are simply (i) the percentage contribution of the selected events to the overall integral of the distribution and (ii) the percentage contribution of the selected events to the integral of the positive portion of the distribution. Depending on the season and hemisphere, these values range from about 13% to over 16%. As almost all the zonally integrated transport values are positive, the overall and poleward-only contributions are almost identical.

As a point of comparison, the last column in Table 3 shows the contributions found for the local extremes relative to the single-point PDFs. Compared with these, the contributions of the zonal case may seem extremely small. However, one should keep in mind that this is somewhat expected. Indeed, the local extremes correspond to specific circulation patterns that have the ability to effect an enormous heat transport. This can be orders of magnitude larger than the typical values at a given point (MC13). In the zonal picture, however, it is hard to imagine planetary-scale coherent structures that could account for a similar effect.

It is also instructive to compare the values shown in Table 3 to the weight of the corresponding events in a Gaussian distribution. To obtain these values, Gaussian profiles with the same means and standard deviations as the zonal transport distributions are constructed. The role of the velocity and MSE anomalies in driving the transport is not considered here. The portions of the Gaussian distributions above the respective 95th percentiles are then selected, and their weight relative to the integral of the positive portion of the Gaussians is computed as a percentage. The resulting values are shown in the third data column of Table 3. Even though these values appear to be similar to those found for the reanalysis distributions, a random Monte-Carlo sampling procedure shows that the differences are statistically significant at the 99% confidence level for all four season–hemisphere combinations. There is therefore some basis for calling the top percentiles of the zonally integrated transport distributions 'zonal extremes'.

5. Zonal *versus* local extremes

Having established that there is reason to discuss zonal extremes, the next pertinent question to address is how these zonal events might relate to the local extremes analysed in section 3 of this article. The terminology 'zonal extremes' refers to the top 5% of events in the PDFs of the zonally integrated meridional heat transport.

5.1. *A pictorial overview*

A first overview of the relationship between local and zonal heat transport can be gleaned from a simple comparison of the frequencies of local and zonal extreme events on a given latitude circle over a season. The plots for five consecutive DJF seasons (1989–1994) are shown in Figure 9. The figure refers to the 50°N latitude circle. The choices of season, years and latitude are entirely random, as the plot simply serves to illustrate the typical pattern seen throughout the period and domains analysed in the present article. On a given day, the value of the vertical bar is set to the number of local $v'H'$ events falling in the top five percentiles of the local heat transport distribution for the full Northern Hemisphere domain. The vertical lines over the light grey bars mark the days on which a zonal extreme occurs at the selected latitude. Again, these are defined as the top five percentiles of the zonal distribution for the full Northern Hemisphere domain.

The local extreme events tend to happen in bursts lasting for a few days, during which very significant numbers of events occur. In the context of the circulation features highlighted in section 3 these could correspond, for example, to periods of particularly vigorous synoptic activity in the storm tracks (e.g., Pinto *et al.*, 2014). The bursts are preceded and followed by days with very little activity. In certain years, more extended periods of activity are present. At the same time it is clear that, at least at the selected latitude, there is a continuous background of extremes throughout the season. The intermittency in the frequency of the local extremes is consistent with the link found between local transport extremes and circulation structures typically associated with the storm tracks. In fact, the intermittent nature of eddy activity in the storm tracks is well known and can be captured by simple models (e.g., Ambaum and Novak, 2014).

Shifting the attention to the zonal extremes, it can be seen that they typically match the periods of strong local activity. However, there are also periods with an enhanced local extreme event

Table 3. Percentage contributions of the top five percentiles of $v'H'$ events in DJF and JJA to the net and poleward-only meridional atmospheric heat transport due to transient eddies. The first three data columns refer to zonally integrated values; the last column to single grid box values. The 'Gaussian equivalent' column indicates the positive-only contributions of events above the same percentile thresholds as the extremes, in Gaussian distributions with the same means and standard deviations as the reanalysis distributions. The data cover the same range as in Table 2.

Hemisphere	Season	Zonal integration % weight			Local events % weight
		Net	Poleward-only	Gaussian equivalent	Net
Northern	DJF	16.2	16.0	13.6	56.8
	JJA	15.2	15.1	12.9	61.8
Southern	DJF	16.3	16.3	13.9	52.7
	JJA	13.3	13.3	12.8	43.6

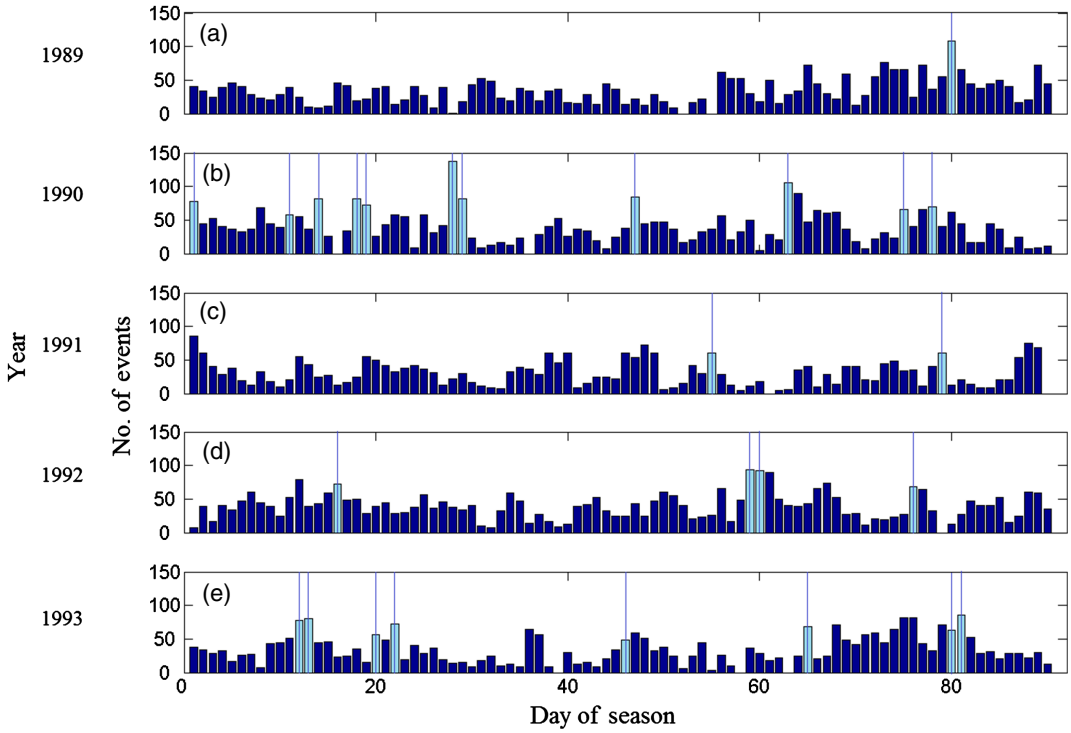

Figure 9. Bar plot of local and zonal extreme event frequency along the 50°N latitude circle. The data cover the 850 mb fields. Both local and zonal extremes are defined as events in the top 5 percentiles of the respective meridional heat transport distributions for the full Northern Hemisphere domain. The five panels (a) to (e) correspond to DJF seasons from December 1989 to February 1994. The height of the bars corresponds to the number of longitude grid boxes displaying a local extreme event on a given day; vertical lines over the light grey bars mark days where the 50°N latitude circle displays a zonal extreme event. The abscissa indicate the day of the season.

frequency that do not match any zonal extremes, and vice versa. This visual appraisal of the temporal variability of meridional heat transport therefore suggests a strong link between local and zonal extreme events, but also highlights that there might be other mechanisms at play.

5.2. *Local and large-scale drivers*

Based on the visual overview provided by Figure 9, we formulate the following three hypotheses concerning the origin of large values of zonally integrated heat transport:

a. They are due to several synchronized local extremes at a given latitude. Namely, several single grid box extreme events occurring on the same day, at the same latitude. These local extremes might correspond to either:
   (i) a large number of well-separated peaks in heat transport or;
   (ii) one or more zonally elongated regions of large transport values that register as local extremes at multiple locations.

b. They are due to an above-average transport across a very large number longitudes, with no significant contribution from the local extremes. That is, to a generalized increase in the transport across large stretches of a latitude circle, without necessarily implying a higher than normal frequency of extreme events at fixed locations.

c. A combination of points:
   (i) a(i) and (b) or;
   (ii) a(ii) and (b).

A pictorial schematic of hypotheses (a) and (b) is provided in Figure 10.

The barplot in Figure 9 indicates that both (a) and (c) are plausible answers. The results from section 3 further suggest that it would be natural for large heat transport bursts to be spread out over multiple longitudes (and not single unrelated points). In fact, a large portion of the heat transport in the midlatitudes is driven by baroclinically unstable waves, and a synoptic or mesoscale eddy will cover several grid boxes. The zonal profiles, such as that shown in Figure 1, indeed suggest that the central core of a local heat transport extreme typically covers a few degrees longitude. Therefore, a local extreme will often be part of a larger longitudinal band of strong heat transport, and not an isolated burst. This would correspond to case a(ii) above. However, several low-pressure systems typically coexist around a given latitude circle, making case a(i) equally credible. Hypothesis (c) is essentially a relaxed version of (a), and is therefore also plausible following the above arguments.

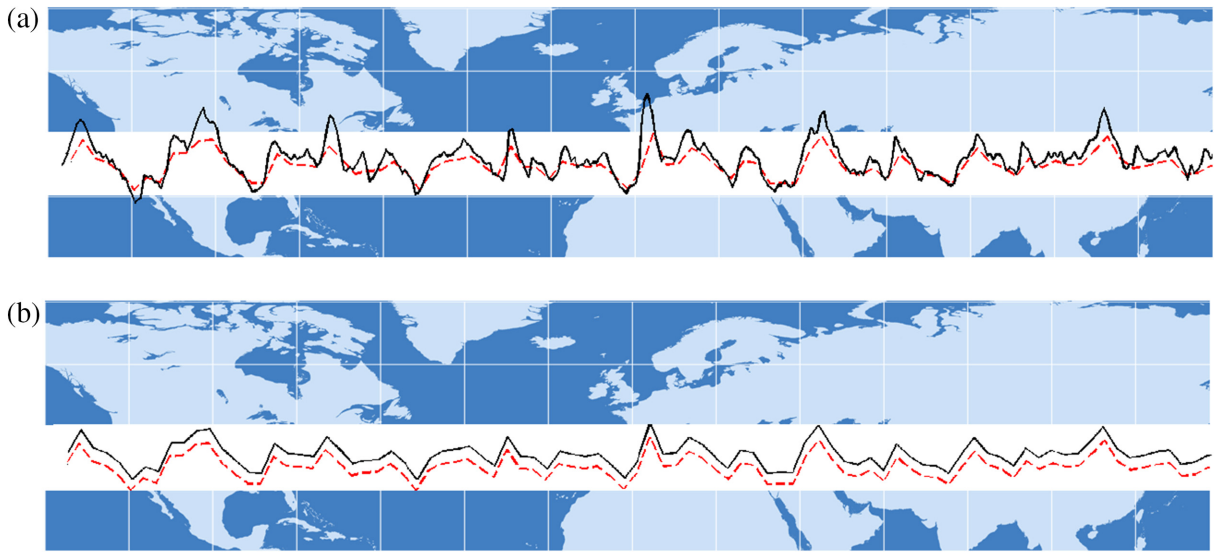

Figure 10. Schematic illustrating hypotheses (a) and (b) formulated in section 5.2. The dashed curves in both panels represent a hypothetical baseline meridional heat transport profile at a given latitude. The continuous curve in (a) represents an enhanced heat transport (zonal extreme) resulting from strong, localized increases at specific locations (local extremes). The continuous curve in (b) represents an enhanced heat transport (zonal extreme) resulting from an approximately uniform increase at all longitudes, without any large local peaks.

At the same time, Messori and Czaja (2014) found that long length scales and time periods, beyond those typically associated with baroclinic motions, play an important role in the power spectra of meridional heat transport by transient motions. This points to the possibility that a larger than average transport across a broad range of longitudes might also contribute to the zonal extremes. Moreover, the analysis in section 5.1 confirms that there are instances where the frequencies of local and zonal extremes appear to be decoupled. Hence, even though hypotheses (a) and (c) remain the most likely, it is not possible to exclude *a priori* case (b).

5.3. *The role of local extremes*

A robust test of hypothesis (a) first of all requires verification of whether any zonal extremes correspond to no local extremes. It is found that, for all season–hemisphere combinations, virtually all of the zonal extremes correspond to at least one local extreme. That is, when meridional heat transport around a given latitude on a given day classifies as a zonal extreme, there is at least one location at that latitude where the transport also classifies as a local extreme. For non-extreme zonal days, the picture is very different. Depending on the hemisphere and season, between 20 and 39% of non-extreme zonal data points correspond to no local extremes. The percentages are systematically higher for the Southern Hemisphere, where, as illustrated in Figure 6(a), the bulk of the local extremes is centred on a narrow band in the Southern Ocean, and there are very few extremes in the high latitudes. According to hypothesis (b), an increase in the zonally integrated meridional heat transport should not imply a higher than normal frequency of extreme events at fixed locations. The large discrepancy found between extreme and non-extreme zonal days therefore supports hypotheses (a) and (c).

The next natural step is to investigate what happens when there are local extremes at a given latitude. To this end one can produce PDFs of the number of local extremes around a full latitude circle on days corresponding to zonal extremes and on all other days, excluding days/latitudes with no local extremes. If zonal extremes come about because of local extremes, then the PDFs for the extreme zonal days should peak at significantly larger values than those for all other days. Panels (a) and (b) in Figure 11 show the resulting PDFs for Northern Hemisphere DJFs and Southern Hemisphere JJAs, respectively. White bars correspond to data for zonal extremes, while grey bars correspond to data for all other days. The dataset used has 512 grid boxes around each latitude circle; this number clearly provides an upper bound on the number of simultaneous local extremes that can occur at a given latitude. For Northern Hemisphere DJF, the extreme PDF's MLV and mean are both larger than that of the non-extreme PDFs by a factor of approximately two. The distributions for Southern Hemisphere JJA (Figure 11(b)), Northern Hemisphere JJA and Southern Hemisphere DJF (not shown) present a similar pattern. In all four season–hemisphere combinations, the PDFs for extreme and non-extreme zonal days are statistically different under a two-sample Kolmogorov–Smirnov test, with the null hypothesis of the same parent distribution rejected at the 5% significance level.

Hypothesis (a) above would imply that the two PDFs have almost no overlap, because local extremes would be the sole drivers of zonal ones. In contrast, hypothesis (b) would correspond to approximately equal PDFs for both extreme and non-extreme zonal days. Even though the distributions in Figure 11 are statistically different, there is still considerable overlap between them. To quantify this statement, the overlap between the extreme and non-extreme PDFs in panels (a) and (b) of Figure 11 is 31 and 32%, respectively. These are simply the percentages of data points in the distributions that lie in the overlapping portions of the different bins. They provide an indirect measure of how likely it is for an extreme zonal day to have the same number of local extreme events as a non-extreme zonal day. It should further be remembered that the distributions only refer to those day/latitude points that display at least one local extreme. As previously discussed, a significant portion of the non-extreme zonal data corresponds to instances when no local extremes are seen. In physical terms, the above results correspond to a scenario governed by the number of local events, with a significant contribution from changes in the background flow (hypothesis c) above).

5.4. *Clustering of local extremes*

In terms of the local extremes, hypothesis (c) considers two options: (i) that they are driven by independent atmospheric systems; or (ii) that they form part of large-scale coherent transport structures. To distinguish between the two, a decorrelation length for the heat transport is computed; local extremes separated by less than one decorrelation length are counted only once (see section 2.2 for details). This process reduces the local extremes to around 8% of their original numbers. The severe decrease is partly due to the fact that local extremes

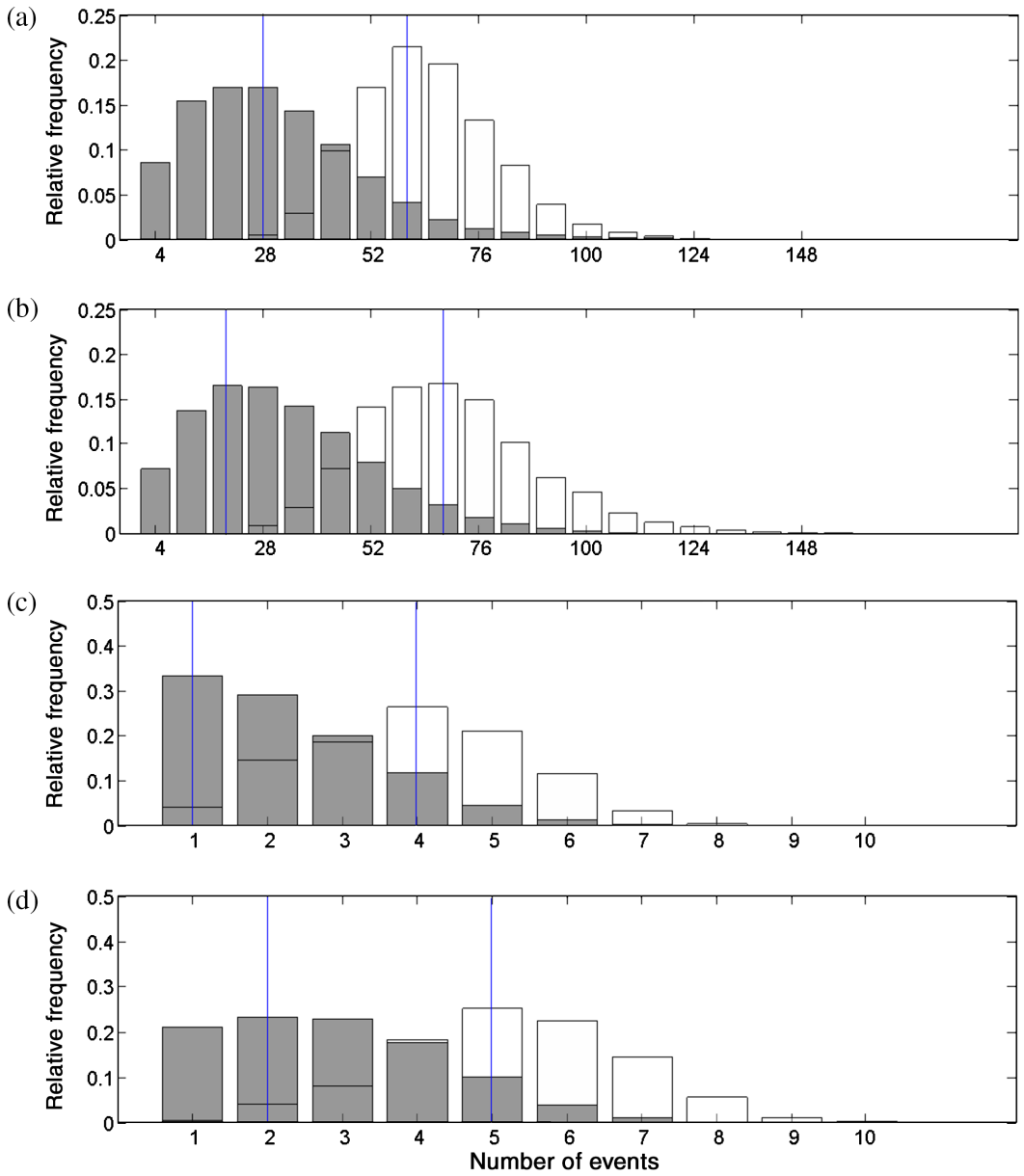

Figure 11. The PDFs of the number of local extreme events around a full latitude circle for days that are in the top 5% (white) and days that are in the bottom 95% (grey) of the distributions of the zonally integrated meridional atmospheric heat transport due to transient eddies. The PDFs cover (a,c) Northern Hemisphere DJF and (b,d) Southern Hemisphere JJA data, over the same temporal and spatial range as Figure 7. (a) and (b) consider all local extremes; (c) and (d) only count well-separated local extremes. Only days/latitudes with at least one local extreme are considered. The most likely values are respectively (a) 60 (extremes, in white) and 28 (non-extremes, in grey), (b) 68 and 20, (c) 4 and 1 and (d) 5 and 2. The corresponding means are respectively (a) 64 and 31, (b) 70 and 33, (c) 4.0 and 2.3 and (d) 5.2 and 2.9. The vertical lines show the bins corresponding to the most likely values.

extend across several grid boxes, as seen in section 3. A single local maximum will therefore be counted multiple times if the selection is purely based on the exceedance of a threshold. The rest of the decrease can be ascribed to multiple closely spaced local extreme peaks which form part of a single, extensive band of strong meridional heat transport, and are counted only once. The local extremes therefore present a pronounced clustering, corresponding to hypothesis c(ii). This is in agreement with the well-defined geographical regions of high extreme event frequency shown in Figure 6(a).

The fact that clusters of local extremes exist, however, does not necessarily mean that they actively drive the zonal extremes. Indeed, the clustering might be a general property of the local heat transport, and be completely unrelated to the zonal extremes. We therefore test whether there is any systematic relationship between the additional heat transport seen on extreme zonal days and the size and/or number of clusters of local extremes. To do this, the PDF analysis described in section 5.3 above is repeated for the new set of well-separated local extremes. Panels (c) and (d) in Figure 11 display the results for Northern Hemisphere DJF and Southern Hemisphere JJA, respectively. As before, the extreme zonal days display systematically more local extremes than the non-extreme zonal days. The distributions are again statistically different under a two-sample Kolmogorov–Smirnov test, at the 95% confidence level, for all hemispheres and seasons. However, it is immediately noticeable that the overlap between the distributions for the extreme and non-extreme zonal days is much larger than before. The overlaps are now 55% for Northern Hemisphere DJF (panel (c)) and 46% for Southern Hemisphere JJA (panel (d)). If the additional heat transport during extreme zonal days was entirely due to larger clusters of local events, the two PDFs in each of the panels would overlap completely. In fact, each cluster would be counted only once, regardless of the number of local extremes forming it. The opposite would occur if the additional transport were exclusively due to a larger number of clusters.

5.5. *The weak synchronisation hypothesis*

The picture that emerges from the above analysis corresponds to a zonally integrated heat transport that is largely, but not

exclusively, governed by the number of local extreme events. It is further found that the local extremes driving the transport tend to cluster in zonally elongated bands. This corresponds to hypothesis c(ii) of the original list. If local extremes forming part of the same cluster are counted only once, approximately half the extreme zonal days have the same number of clusters as the non-extreme ones. This indicates that a zonal extreme may come about because of either more frequent or larger clusters of local extremes (or indeed both).

We therefore conclude that the zonal heat transport is characterized by a *weak synchronization* effect, whereby zonal extremes are partly driven by synchronized, zonally elongated bands of local extremes. However, the zonal extremes have a much weaker impact on the overall transport distribution than their single-point counterparts, as shown in section 4.3.

Finally, it should be noted that there is a caveat to the methodology adopted here. The validity of the hypotheses made above may depend on the exact definition of local extremes in terms of percentiles of a distribution. Indeed, if the percentile threshold were to be changed by tens of percentiles, the picture would in turn change. However, the circulation maps shown in section 3 are specific to only the strongest transport events, suggesting that data points above the 95th percentile are physically different from the norm. This threshold is therefore a suitable selection criterion. Although it could be argued that the 93rd or 97th percentiles would be equally valid choices, it would be unphysical to choose, for example, the 70th percentile as threshold. Moreover, if the percentiles defining local extremes change, so do those defining the zonal ones. For example, if the local extremes were to be defined as events within the top 10 percentiles of the single-point distribution, the same definition would then be applied to the zonally integrated distribution in order to select the extreme zonal days. This definition is a limit case because, as discussed in section 3, the events selected by this relaxed criterion lack some of the circulation features seen in Figure 1. If such a threshold were adopted, the fractional overlap of the PDFs corresponding to those in Figure 11(a) and (b) would rise from 31 and 32% to 64 and 51% respectively, but the distributions for extreme and non-extreme days would remain statistically different. We therefore conclude that large changes in the chosen extreme event threshold would not be justifiable from a dynamics standpoint, while small changes do not significantly alter the findings discussed here.

6. Further discussion and conclusions

The present article examines zonally integrated meridional atmospheric heat transport due to transient eddies, focusing on low levels in the mid- and high latitudes. Previous studies have already shown that the local transport is very discontinuous in nature, and is very sensitive to a few extreme events every season (e.g., Swanson and Pierrehumbert, 1997; MC13; Messori and Czaja, 2014). Here, it is shown that the local extremes can be associated with precise circulation features. In the storm-track regions, these correspond primarily to WCB-type structures. Different circulation patterns, such as cold air outbreaks, emerge in other regions.

The existence of these circulation analogues for local extremes suggests that there might be a measure of synchronization between extremes at different longitudes, hence giving rise to large values of zonally integrated meridional transport, or zonal extremes. This is indeed seen to be the case: the zonal extremes in the ERA-Interim data are found to be partly due to numerous local extremes occurring simultaneously around a given latitude circle. The local extremes tend to cluster in zonally elongated bands, with a more pronounced clustering during extreme zonal days. In addition to this, the zonal events also display a contribution from increased transport at non-extreme locations. These two features suggest that scales larger than those associated with the extremes act to enhance the transport over wide areas of the latitude circle. Such inference is in agreement with the results of Messori and Czaja (2014), who found that long length scales (zonal wave numbers ≤ 4) and time periods (periods >8 days), beyond those typically associated with baroclinic motions, play an important role in the power spectra of meridional heat transport by transient eddies.

The percentage contributions of zonal extreme events to the net, zonally integrated meridional heat transport are significantly lower than the corresponding values found for local extremes (MC13). They are still, however, significantly larger than those found for Gaussian distributions with the same means and standard deviations as the transport PDFs.

It should also be remembered that the local poleward transport extremes are often associated with a return equatorward transport (see Figure 1). Such return transport is highly variable, and might provide an additional explanation as to why days with a large number of local extremes do not always correspond to zonal extremes. As shown in Figure 11, a small fraction of non-extreme zonal days displays a very large number of local extremes – larger, in fact, than the most likely value for an extreme zonal day. A realistic hypothesis is that these outlying non-extreme days are characterized by local extremes that have uncommonly strong recirculation features, such that their net transport is smaller than usual.

Extending the analysis of recirculation features to a global scale it is interesting to note that, even when considering zonally integrated values, the transport is not always polewards. In fact, the 850 mb zonally integrated transport is negative on a small fraction of the days and latitudes considered. Only a very brief analysis of these events has been performed here. The results suggest that the negative transport is primarily driven by the large-scale motions, associated with time-scales beyond 8 days. This is consistent with the picture of baroclinic-scale growing systems (periods <8 days) mainly accounting for poleward transport values, and the weaker or even negative values corresponding to decaying waves. It is further found that the transport by transient motions displays a high vertical coherence, meaning that when the transport at 850 mb is negative, the transport at upper levels has a significant chance of also being negative. When the net atmospheric energy transport is computed, the other components of the transport (e.g., climatological stationary eddies and/or compensation by a reduced Ferrel cell) often balance out the negative contribution by transient motions. However, there is a small fraction of cases (1–2% of the total) where a negative 850 mb transport corresponds to a negative net transport. On these days, at a given latitude, the atmosphere carries energy towards the Equator. A more in-depth analysis, based on existing studies of the co-variability of the different components of the atmospheric energy transport (e.g., Trenberth and Stepaniak, 2003), would be required in order to determine the dynamical drivers of these events.

Although the general picture seems coherent, there are some aspects that require further clarification. The first is whether the role of the longer time-scales and length scales, mentioned above, is compatible with a direct correspondence between the extremes and the local atmospheric features discussed in section 3. The definition of 'extreme' adopted here is based on a numerical threshold. When considering the spectral features of the heat transport, large variations in power at scales consistent with baroclinic motions could be sufficient to determine whether events with high power at larger scales classify as extremes or not. That is, the power in a specific region of the spectrum could determine whether a given event falls above or below the threshold, even though the said region might not account for the majority of the net spectral power. One can therefore reconcile the spectral and synoptic analyses, and interpret the extreme events as regionally coherent synoptic features superimposed on planetary-scale variability. This view is further strengthened by the fact that the clustering of local extremes is enhanced during zonal extreme days. In fact, the formation of the clusters could be facilitated by an enhanced heat transport driven by planetary-scale modes.

In this regard a detailed spectral analysis, studying the contributions of the different periods to the vertical and zonal

structure of the extremes, could prove valuable. Applying a high-pass or band-pass filter to the data, with an upper cut-off around 6–8 days, would remove the planetary-scale component and highlight the structure of the local synoptic motions.

A second point concerns the differences seen in the zonally integrated transport distributions of the two hemispheres. It has been suggested in section 4 that the bimodality seen in the Southern Hemisphere distribution is the result of two distinct patterns. One holds for the lower latitudes, where there are larger values of zonally integrated transport. The other holds for the higher latitudes, where the zonally integrated transport is smaller. Although, in general, this is also true of the Northern Hemisphere, the two hemispheres display a clear difference in the geographical distributions of the local extremes. In the Northern Hemisphere, the location of the extreme events is varied, with the two storm tracks playing an important role, but with several other areas of vigorous activity at higher latitudes (MC13). This is in contrast to the Southern Hemisphere, where the vast majority of the extreme events is concentrated in a narrow latitudinal band, providing a much sharper contrast between the lower and higher latitudes (see Figure 6(b)).

Regardless of these differences, both hemispheres display a pronounced variability on a zonally integrated level, which translates into the existence of zonally integrated transport extremes. This is very significant for the energy balance of the high latitudes. The past decade has seen an unprecedented sea-ice loss in the Arctic basin, which has been underestimated by almost all climate models (e.g., Stroeve *et al*., 2007). There are studies suggesting that anomalous atmospheric heat transport convergence at the high latitudes might drive a local long-wave forcing, playing a significant role in the melt process (Graversen *et al*., 2011). Further efforts in understanding and modelling the variability of zonally integrated meridional heat transport, coupled with a study of the possible impacts of climate change on such variability, would therefore be crucial in order to better understand the future of the polar regions.

Acknowledgements

During the research, G. Messori has been funded by the UK's Natural Environment Research Council, as part of the RAPID-RAPIT project, and by Sweden's Vetenskapsrådet, as part of the MILEX project. ERA-Interim reanalysis data were obtained from the BADC FTP server at ftp.badc.rl.ac.uk. We thank the anonymous reviewers for the many helpful comments; we also thank C. H. O'Reilly for his suggestions and for editing the article. Finally, we are very grateful to R. G. Graversen for providing the vertically integrated heat transport data and for a stimulating discussion on equatorward transport events.

Supporting information

The following supporting information is available as part of the online article:

File S1. The role of velocity and MSE in driving heat transport extremes.

File S2. Time-filtered heat transport.

References

Ambaum MHP, Novak L. 2014. A nonlinear oscillator describing storm track variability. *Q. J. R. Meteorol. Soc.* **140**: 2680–2684, doi: 10.1002/qj.2352.

Boutle I, Belcher S, Plant R. 2010. Moisture transport in mid-latitude cyclones. *Q. J. R. Meteorol. Soc.* **136**: 1–14.

Browning KA. 1997. The dry intrusion perspective of extra-tropical cyclone development. *Meteorol. Appl.* **4**: 317–324.

Catto J, Shaffrey L, Hodges K. 2010. Can climate models capture the structure of extratropical cyclones? *J. Clim.* **23**: 1621–1635.

Chang EKM. 1993. Downstream development of baroclinic waves as inferred from regression analysis. *J. Atmos. Sci.* **50**: 2038–2053.

Donohoe A, Battisti DS. 2012. What determines meridional heat transport in climate models? *J. Clim.* **25**: 3832–3850.

Eckhardt S, Stohl A, Wernli H, James P, Forster C, Spichtinger N. 2004. A 15-year climatology of warm conveyor belts. *J. Clim.* **17**: 218–237.

Graversen RG. 2006. Do changes in the mid-latitude circulation have any impact on the Arctic surface air temperature trend? *J. Clim.* **19**: 5422–5438.

Graversen RG, Mauritsen T, Drijfhout S, Tjernström M, Mårtensson S. 2011. Warm winds from the Pacific caused extensive Arctic sea-ice melt in summer 2007. *Clim. Dyn.* **36**: 2103–2112.

Hwang Y-T, Frierson DMW. 2010. Increasing atmospheric poleward energy transport with global warming. *Geophys. Res. Lett.* **37**: L24807, doi: 10.1029/2010GL045440.

Kolstad EW, Bracegirdle TJ. 2008. Marine cold-air outbreaks in the future: An assessment of IPCC AR4 model results for the Northern Hemisphere. *Clim. Dyn.* **30**: 871–885.

Lau N-C. 1978. On the three-dimensional structure of the observed transient eddy statistics of the Northern Hemisphere wintertime circulation. *J. Atmos. Sci.* **35**: 1900–1923.

Madonna E, Wernli H, Joos H, Martius O. 2014. Warm conveyor belts in the ERA-interim dataset (1979–2010). Part I: Climatology and potential vorticity evolution. *J. Clim.* **27**: 3–26, doi: 10.1175/JCLI-D-12-00720.1.

Messori G, Czaja A. 2013. On the sporadic nature of meridional heat transport by transient eddies. *Q. J. R. Meteorol. Soc.* **139**: 999–1008, doi: 10.1002/qj.2011.

Messori G, Czaja A. 2014. Some considerations on the spectral features of meridional heat transport by transient eddies. *Q. J. R. Meteorol. Soc.* **140**: 1377–1386, doi: 10.1002/qj.2224.

Nakamura H, Izumi T, Sampe T. 2002. Interannual and decadal modulations recently observed in the Pacific storm track activity and East Asian Winter Monsoon. *J. Clim.* **15**: 1855–1874.

Neelin JD, Held IM. 1987. Modelling tropical convergence based on the moist static energy budget. *Mon. Weather Rev.* **115**: 3–12.

Peixoto J, Oort A. 1992. *Physics of Climate*. American Institute of Physics New York, NY.

Pinto JG, Gómara I, Masato G, Dacre HF, Woollings T, Caballero R. 2014. Large-Scale dynamics associated with clustering of extra-tropical cyclones affecting Western Europe. *J. Geophys. Res. Atmos.* **119**: 13704–13719, doi: 10.1002/2014JD022305.

Simmons A, Uppala S, Dee D, Kobayashi S. 2006. ERA-Interim: New ECMWF reanalysis products from 1989 onwards. *ECMWF Newsl.* **110**: 25–35.

Stroeve J, Holland MM, Meier W, Scambos T, Serreze M. 2007. Arctic sea ice decline: Faster than forecast. *Geophys. Res. Lett.* **34**: L09501, doi: 10.1029/2007GL029703.

Swanson KL, Pierrehumbert RT. 1997. Lower-tropospheric heat transport in the Pacific storm track. *J. Atmos. Sci.* **54**: 1533–1543.

Trenberth KE. 1991. Climate diagnostics from global analyses: Conservation of mass in ECMWF analyses. *J. Clim.* **4**: 707–722.

Trenberth KE, Stepaniak DP. 2003. Covariability of components of poleward atmospheric energy transports on seasonal and interannual timescales. *J. Clim.* **16**: 3691–3705, doi: 10.1175/1520-0442(2003)016<3691:COCOPA>2.0.CO;2.

Zelinka MD, Hartmann DL. 2012. Climate feedbacks and their implications for poleward energy flux changes in a warming climate. *J. Clim.* **25**: 608–624, doi: 10.1175/JCLI-D-11-00096.1.

